



Unraveling a trade-off between positive effect and poisoning mechanism of soot over low-dose PtCu/CeO₂ for simultaneously photothermocatalytic removal of VOCs and soot

Jiejing Kong^{a,b}, Shengnan Song^{a,b}, Weina Zhao^{a,b}, Zijie Yu^{a,b}, Ziwei Xiang^b, Guiying Li^{a,b}, Weiping Zhang^{a,b}, Taicheng An^{a,b,*}

^a Guangdong Key Laboratory of Environmental Catalysis and Health Risk Control, Institute of Environmental Health and Pollution Control, Guangdong University of Technology, Guangzhou 510006, China

^b Guangdong Engineering Technology Research Center for Photocatalytic Technology Integration and Equipment, School of Environmental Science and Engineering, Guangdong University of Technology, Guangzhou 510006, China

ARTICLE INFO

Keywords:

Photothermocatalytic oxidation
VOCs and soot elimination
Adsorption mechanism
Alloy catalysts
Trade-off effect

ABSTRACT

It is challenging for simultaneous removal of VOCs and soot as soot would aggravate coke formation, and the lack of a deep understanding of pollutant effect on catalyst textural properties seriously limit its application. Herein, efficiently photothermocatalytic simultaneous removal of VOCs and soot was achieved by optimizing coke resistance and Pt utilization of PtCu/CeO₂ through alloy modification and oxygen vacancy engineering. The findings of our combined experimental and computational study on catalytic process unravel a trade-off between positive effect and poisoning mechanism of soot, as follow: the unique photothermal properties and enhanced VOCs adsorption of soot accelerate VOCs degradation, while partially degraded soot passivate surface-active site of PtCu/CeO₂ and weaken OH/O₂ adsorption, thus suppressing VOCs mineralization. These new insights into the interfacial mechanism will provide a promising strategy to catalytic performance optimization and practical application.

1. Introduction

Great changes have been taken in the energy consumption structure of today's world, but carbonaceous fuels still play a crucial role in the energy sectors [1]. In the process by which fuel is combusted to release the energy stored in chemical bonds, both pyrolysis and incomplete combustion of carbon-containing fuels ubiquitously take place, leading to the formation and emission of mutagenic and carcinogenic VOCs and soot [2]. VOCs consist of a group of substances characterized by high vapor pressure at low temperatures, and energy industrial VOC emissions in China are mainly alkanes with particularly stable C-H bonds and low polarity, such as cyclohexane [3,4]. Soot particle form in highly inhomogeneous and changing conditions from the combustion process, its composition is quite variable, mainly including amorphous carbon, graphite, fullerenes, and hydrocarbons [5]. The simultaneous release of VOCs and soot into atmosphere has had strong environmental impacts and severely threatened human health because of their toxicity and

involvement in formation of photochemical smog and hazy [6]. However, simultaneous removal of VOCs and soot is still rather challenging, as most of them are very stable and often undergo incomplete oxidation, even producing undesirable byproducts with much higher toxicities than the original ones.

Recently, photothermocatalytic oxidation is emerged as an attractive solution due to its high destruction efficiency and moderate operating temperature by synergistic enhancement of photo and thermal catalysis during reaction [7–9]. The corresponding catalysts require not only superior low temperature catalytic activity but also long durability. CeO₂ supported noble metal catalysts have been extensively applied in VOCs degradation owing to their high oxidation activity at low oxidation temperature [10–12], but also limited by high cost and low stability [13]. It is reported that oxygen vacancies of the support can provide sites for anchoring and high dispersion of noble metals, which contributed to utilization of noble metal atoms, thereby reducing their load and cost [14]. As for the poor stability of supported noble metal catalyst, the

* Corresponding author at: Guangdong Key Laboratory of Environmental Catalysis and Health Risk Control, Institute of Environmental Health and Pollution Control, Guangdong University of Technology, Guangzhou 510006, China.

E-mail address: antc99@gdut.edu.cn (T. An).

<https://doi.org/10.1016/j.apcatb.2023.123118>

Received 7 June 2023; Received in revised form 15 July 2023; Accepted 17 July 2023

Available online 18 July 2023

0926-3373/© 2023 Elsevier B.V. All rights reserved.

main reason is due to rapid VOC degradation in photothermocatalytic reaction, part of carbon species generated from alkanes pyrolysis fail to participate in instant oxidation reaction, especially at low temperature, resulting in easy coverage of coke on catalyst surface, and subsequently causing catalyst deactivation [15,16]. Besides, coke and soot are similar in formation, but soot is easy to adsorb intermediates because of its porous structure, thus prone to cause aggregation of carbon species, aggravating coke formation [17]. In this regard, the development of CeO₂ supported noble metal catalyst with a high coke resistance is therefore highly essential for further advancing its high efficiency and stable application in simultaneously photothermocatalytic degradation of VOCs and soot. For the supported noble metal catalyst, there are three main factors that affect coke formation, including: (1) About noble metal. Since a relatively large-sized metal active structure is generally required in nucleation of coke, reducing the size of noble metal can inhibit coke formation [18,19]. In addition, an excessively high loading of noble metal makes a dense active site participate in more catalytic reactions, which is easy to lead to rapid accumulation of coke [20]. (2) About support. As a strong acid site is more likely to cause carbon polymerization [21], weakening surface acidity of support can effectively inhibit nucleation and growth of carbon species. Many studies have accepted that oxygen vacancies can act as Lewis acid sites to create weak acid sites, thus inhibiting carbon deposition [14,22]. (3) Interaction between noble metal and support. A strong metal–support interaction (MSI) could lower metal mobility on support surface, generate highly dispersed active phases and metal active structure with a smaller size, and inhibits dissociation and dehydrogenation of hydrocarbon molecules, thus reducing coke formation [23]. In this context, constructing CeO₂ supported low-dose PtCu ultrafine alloy catalyst with abundant oxygen vacancies is expected to be a high coke-resistance and low cost photothermocatalyst, as alloying could not only allow to minimize amount of Pt used and decrease its nanoparticle size [24], but also strengthen MSI [25], and oxygen vacancies of the support could inhibit coke formation.

In addition to constructing active alloy catalyst, tracking effect of pollutant on catalyst textural properties during photothermocatalytic process plays a prominent role in providing a strategy to further enhance its catalytic performance. Notably, soot would not only aggravate coke formation in photothermocatalytic reaction, but also prone to occupy active site of catalyst and then passivate its surface state, just as coke increasing, thus poisoning catalyst [26]. On the other hand, when soot is exposed to atmosphere, a large number of polar and oxidizing oxygen-containing functional groups will be derived from amorphous carbon and organic carbon on its surface [27], and then a wealth of surface-active sites for generating reactive oxygen species (ROs) will be formed [28,29], together with its unique properties of light absorption and heat transfer [30], soot could also promote photothermocatalytic oxidation. Therefore, it is necessary to investigate the trade-off between positive effect and poisoning mechanism of soot on the used catalyst, to optimize photothermocatalytic process parameters for realizing high efficiency and high stability of simultaneous removal of VOCs and soot.

In this work, low-dose PtCu ultrafine alloys were stabilized by CeO₂ with abundant oxygen vacancies to create a strong MSI, which makes the as-prepared PtCu/CeO₂ possess high coke resistance, stability, and high reactivity for simultaneously photothermocatalytic removal of cyclohexane and soot. Comparison was made against a reference PtCu supported on Al₂O₃. PtCu/CeO₂ were characterized by a host of techniques to determine their structure, morphology, composition, and textural properties. Most importantly, XPS, *in-situ* cyclohexane-TPD, and DFT calculations were also employed to investigate effect of soot on the element's valence states and surface oxygen species types of PtCu/CeO₂, as well as adsorption, desorption and oxidation mechanisms of cyclohexane on PtCu/CeO₂ surface, to identify soot's positive and negative role in simultaneously photothermocatalytic removal of VOCs and soot over this newly-prepared PtCu/CeO₂, and then understand the underlying reaction mechanism.

2. Experimental section

2.1. Synthesis of PtCu nanoparticles

Different atomic ratios of PtCu nanoparticles (Pt/Cu molar ratio is respectively close to 1:1, 1:3 and 1:9) were prepared from stock solutions of Pt and Cu precursor salts. In a typical synthesis, 10.3 μmol of H₂PtCl₆·6 H₂O and appropriate Cu(CH₃COO)₂·H₂O were dissolved in 20 mL of oleylamine (OAm) through a combination of ultrasonication to obtain metal precursor stock solutions, and then added to a 100 mL round-bottomed flask. An additional 20 mL of ethylene glycol was added with vigorous mixing using a magnetic stirrer. The resulting mixture was subsequently bubbled with high-purity Ar for 1 h in order to remove dissolved O₂ from solution, then sealed and placed in a 180 °C oil bath to react for 1 h. Afterward, the flask was removed from the heat and allowed to cool to room temperature while still sealed under a high-purity Ar atmosphere. The product nanoparticles were collected by centrifugal separation (at 10,000 rpm for 20 min) and subsequently purified in the following steps: The nanoparticles were dispersed into 30 mL absolute ethyl alcohol (EtOH), and centrifuged after ultrasonication. The precipitated nanoparticles were then redispersed into 30 mL hexanes *via* brief ultrasonication and shaking before being again precipitated and centrifuged. After this second centrifugation cycle, the precipitated nanoparticles were rinsed with EtOH for three times, and then redispersed into 15 mL n-butylamine for the following use.

2.2. Synthesis of PtCu/CeO₂ catalysts

The CeO₂ support used here was obtained by treating commercial CeO₂ through the following process: Reduced it in the humid H₂/N₂ (volume ratio = 1:1) atmosphere at 400 °C for 2 h (humid condition was achieved with N₂ flow into the ultrapure water at 30 °C, relative humidity = 30%), and then annealed it in the N₂ atmosphere at 400 °C for 1 h, followed by calcining in the air/N₂ (volume ratio = 1:1) atmosphere at 400 °C for another 2 h to obtain the final CeO₂ support. Subsequently, 1.0 g CeO₂ was dispersed into the n-butylamine solution comprising PtCu nanoparticles (Pt/Cu molar ratio is 1:1), and the suspension was vigorously stirred magnetically for 24 h in the dark. Thereafter, the resultant product was centrifuged and washed for several times, dried overnight at 60 °C in a vacuum oven, and finally annealed at 400 °C for 2 h under air flow. The final concentration of Pt in the samples was confirmed to be 0.2 wt% by ICP-MS, and Pt/Cu molar ratio was close to 1:1.

2.3. Synthesis of PtCu/Al₂O₃ nanoparticles

The Al₂O₃ support used in this work was obtained by calcining commercial α-Al₂O₃ in air at 900 °C for 6 h. A series of PtCu/Al₂O₃ with 0.2 wt% Pt loadings was obtained *via* an impregnation method. In a typical preparation, 1.0 g Al₂O₃ was dispersed into the abovementioned n-butylamine solution containing PtCu nanoparticles (The molar ratio of Pt to Cu is 1:1, 1:3 and 1:9) under vigorous magnetic stirring in the dark for 24 h. The precipitate was collected by centrifugal separation and washed with absolute ethanol several times, then dried at 60 °C in a vacuum oven overnight, and finally annealed at 400 °C for 2 h under air flow. The as-prepared catalysts were respectively denoted as PtCu, Pt₁Cu₃ and Pt₁Cu₉ for simplicity, and the final content of Pt in all the samples detected by inductively coupled plasma mass spectrometry (ICP-MS, ICAP RQ) is close to 0.2 wt%.

2.4. Catalysts characterization

The morphology, structure, and composition of the materials were characterized by transmission electron microscopy (TEM, 200 kV, Talos-F200S, FEI), X-ray diffraction (XRD, D8 ADVANCE, Bruker) and X-ray photoelectron spectroscopy (XPS, Escalab 250Xi, Thermo Fisher). The

optical properties of the catalysts were measured on UV-vis spectrophotometer (DRS, Agilent Cary 300) and fluorescence spectrophotometer (PL, Fluorolog-3, HORIBA Instruments Incorporated) with a xenon lamp (excitation wavelength 280 nm) as light source. Thermogravimetric (TG) analysis of the soot was carried out in flowing dry air with heating rate of $5\text{ }^{\circ}\text{C min}^{-1}$ from $30\text{ }^{\circ}\text{C}$ to $800\text{ }^{\circ}\text{C}$ by a thermogravimetric analyzer (TGA2, Mettler Toledo). Temperature-programmed reduction of H_2 (H_2 -TPR), temperature-programmed desorption of O_2 (O_2 -TPD) and NH_3 (NH_3 -TPD) were investigated using TP-5078 Autochem-absorption analyzer (Xianquan Industrial and Trading Co., Ltd.), with approximately 20 mg of catalysts loaded in a quartz tube. Prior to each test for H_2 -TPR, the catalyst was pretreated under high-purity N_2 at $30\text{ }^{\circ}\text{C}$ for 1 h, then heated from $30\text{ }^{\circ}\text{C}$ to $780\text{ }^{\circ}\text{C}$ at $12\text{ vol\% H}_2/\text{N}_2$ atmosphere with a flow rate of 30 mL min^{-1} in the dark or under simulated solar irradiation. The illumination condition was achieved by equipping the furnace with a small window on its one side and 300 W Xe lamps on the outside. The consumption of H_2 was detected using a thermal conductivity detector (TCD); For O_2 -TPD experiment, 20 mg of the samples were pretreated at $50\text{ }^{\circ}\text{C}$ for 1 h under high-purity Ar flow, then exposed to high-purity O_2 with a flow rate of 30 mL min^{-1} for 1 h, followed by purged with high-purity Ar to remove physically adsorbed O_2 . O_2 -TPD profile was recorded from $30\text{ }^{\circ}\text{C}$ to $800\text{ }^{\circ}\text{C}$ at a heating rate of $10\text{ }^{\circ}\text{C min}^{-1}$ under Ar flow by TCD detector; Prior to each NH_3 -TPD run, the catalyst was pretreated under high-purity N_2 at $90\text{ }^{\circ}\text{C}$ for 1 h, then turned the flow of $10\text{ vol\% NH}_3/\text{N}_2$ into the system with a flow rate of 30 mL min^{-1} for 1 h. After that, the catalyst was flushed with high-purity N_2 to remove physically adsorbed NH_3 on the catalyst surface. Finally, the system was heated to $700\text{ }^{\circ}\text{C}$ at a heating rate of $10\text{ }^{\circ}\text{C min}^{-1}$, and the NH_3 desorption profiles were recorded under N_2 flow by TCD detector. Temperature-programmed desorption of cyclohexane (Cyclohexane-TPD) and CO (CO-TPD) was measured by PCA-1200 Autochem-absorption analyzer (Beijing Builder Electronic Technology Co. Ltd, China), and one side of the furnace was provided with a window through which light could irradiate. For Cyclohexane-TPD experiment, prior to the test, 50 mg of catalyst were pretreated at $150\text{ }^{\circ}\text{C}$ for 1 h under high-purity He flow, then exposed to 500 ppm cyclohexane/He with a flow rate of 30 mL min^{-1} for 1 h at $30\text{ }^{\circ}\text{C}$ or $150\text{ }^{\circ}\text{C}$. After that, the catalyst was flushed with high-purity He at the corresponding temperature ($30\text{ }^{\circ}\text{C}$ or $150\text{ }^{\circ}\text{C}$) to remove physically adsorbed cyclohexane on the catalyst surface, and then Cyclohexane-TPD profile was recorded from $30\text{ }^{\circ}\text{C}$ to $780\text{ }^{\circ}\text{C}$ at a heating rate of $10\text{ }^{\circ}\text{C min}^{-1}$ under He flow and simulated solar irradiation by TCD detector. For CO-TPD test, 50 mg of the samples were pretreated at $150\text{ }^{\circ}\text{C}$ for 1 h under high-purity Ar flow, then exposed to 10 vol\% CO/Ar with a flow rate of 30 mL min^{-1} at $50\text{ }^{\circ}\text{C}$ for 1 h, followed by purged with high-purity Ar to remove physically adsorbed CO. O_2 -TPD profile was recorded from $50\text{ }^{\circ}\text{C}$ to $800\text{ }^{\circ}\text{C}$ at a heating rate of $10\text{ }^{\circ}\text{C min}^{-1}$ under Ar flow by TCD detector.

2.5. Activity test for VOC degradation

Photothermocatalytic degradation reactions were conducted in a quartz tubular tube (i.d. = 6 mm) fixed-bed reactor (HUASI, China), whose schematic representation has been reported in our previous work [22], and the catalyst can be irradiated through a small window on the one side of the furnace. The simulated solar irradiation came from 300 W Xe lamp ($\lambda = 300\text{--}780\text{ nm}$, optical power density is 200 mW cm^{-2}) (Zhongjiao-jinyuan Science and Technology Co. Ltd., China). Approximately 100 mg catalyst was packed in the reactor. The vapor of cyclohexane was generated by passing N_2 at a certain flow rate through the corresponding solution ($\geq 99\%$), thereafter the vapor was mixed with dry air to achieve $\sim 30\text{ ppm}$ of cyclohexane, and the initial amount of CO_2 is negligible. Gas hourly space velocity (GHSV) value of $30,000\text{ mL h}^{-1}\text{ g}^{-1}$ and humidity of 10% was tested. The concentrations of cyclohexane and CO_2 were respectively measured using the gas chromatography GC9800 (FID) and GC9800 (FID, equipped with a Ni catalyst based methanizer), and detail analysis process has been reported in our

previous work [22]. Five concentration data were measured at each temperature with around a 10 min interval. The concentration data adopted showed less than 10% difference from other measured data at each temperature. The mineralization of cyclohexane was assessed by the following equations:

$$\text{Cyclohexane Mineralization\%} = \frac{[\text{CO}_2]_{\text{out}}}{6[\text{C}_6\text{H}_{12}]_{\text{in}}} \times 100\% \quad (1)$$

where $[\text{C}_6\text{H}_{12}]_{\text{in}}$ are the inlet molar quantity of vaporous cyclohexane, $[\text{C}_6\text{H}_{12}]_{\text{out}}$ and $[\text{CO}_2]_{\text{out}}$ are the outlet molar quantity of vaporous cyclohexane and CO_2 , respectively.

To explore the intrinsic activity of catalysts, the apparent activation energy (E_a) should be calculated according to the linear-fitting Arrhenius equation [15], as followed:

$$\ln Y = \ln(K_r^0 m_{\text{cat}}) - \frac{E_a}{RT} \quad (2)$$

where

$$Y = \frac{\phi_0}{RT_0} \ln\left(\frac{y_{\text{in}}}{y_{\text{out}}}\right) \quad (3)$$

Here K_r^0 is the reaction constant ($\text{mol Pa}^{-1}\text{ g}^{-1}\text{ s}^{-1}$), m_{cat} is the catalyst mass in the reactor (g), E_a is the activation energy (J mol^{-1}), T_0 is the standard temperature (273.15 K), y_{in} and y_{out} are the n-pentane molar fractions at the reactor inlet and outlet, respectively, and ϕ_0 is the feed flow rate under normal conditions ($\text{m}^3\text{ s}^{-1}$). By plotting $\ln Y$ vs. $1/RT$, E_a value can be obtained by the least-squares fitting method.

2.6. Activity test for simultaneous VOCs and soot removal

The composition of the model soot [31] determined by elemental analyzer (Vario EL cube, Elementar) is consisted of 91.0% C, 3.5% O, 1.0% H, 1.0% S, 0.5% N and 3.0% others. Prior to catalytic activity test for simultaneous VOCs and soot removal, 100 mg catalyst and 1 mg commercial soot particles were mixed gently with a spatula (loose contact mode), and then the mixture was placed in the fixed-bed reactor mentioned above. The initial concentration of cyclohexane vapor was $\sim 30\text{ ppm}$, with GHSV value of $30,000\text{ mL h}^{-1}\text{ g}^{-1}$ and humidity of 10%. Catalytic activity tests were carried out by heating the reactor bed from 30° to 450°C at a rate of $1\text{ }^{\circ}\text{C min}^{-1}$. The concentrations of cyclohexane and CO_2 were measured by GC9800 with around a 10 min interval.

2.7. Computational method for DFT calculations

DFT calculations were performed by using the Vienna *ab-initio* simulation package (VASP), while the projector-augmented wave (PAW) method was used to describe the interactions between frozen cores and valence electrons. The electron exchange-correlation was treated by the generalized gradient approximation (GGA) with the Perdew-Burke-Ernzerhof (PBE) functional. The kinetic energy cutoff for the plane-wave basis set was used by 400 eV. The stoichiometric CeO_2 [111] surface was represented by a (4×4) slab model, comprising of 48 Ce atoms and 96 O atoms. To avoid the interactions between periodic slabs, a vacuum space of 15 \AA was added on top of the surface. During geometry optimization, two topmost triatomic layers were fully relaxed, whereas the one bottom layer was kept fixed. The adsorption energy of each chemical species on CeO_2 [111] surface was calculated as:

$$E_{\text{ads}} = E_{\text{species/surface}} - (E_{\text{species}} + E_{\text{surface}}) \quad (4)$$

where $E_{\text{species/surface}}$ was the total energy of species/surface complex, and E_{species} and E_{surface} were the total energy of corresponding species and surface, respectively. The more negative value from this equation indicated the stronger adsorption.

3. Results and discussion

3.1. Physicochemical structural characterization

The physicochemical structure of PtCu/CeO₂ was investigated and compared with that of pure CeO₂ and PtCu catalyst, which loaded PtCu onto inactive Al₂O₃. The actual Pt loading of both PtCu/CeO₂ and PtCu were confirmed to be ~0.2 wt% by ICP-MS, and Pt/Cu molar ratio was close to 1:1. Compared with CeO₂, the characteristic XRD peaks of PtCu/CeO₂ shifted 0.2° towards higher angle, indicating a contraction of the Ce lattice [32], which may be caused by Pt/Cu atoms partially incorporated into the CeO₂ crystal lattice to form Pt-Cu-CeO_x solid solutions (Fig. S1). BET characterization verified this low-dose PtCu did not block the meso- and micropores of CeO₂ (Table S1). Besides, according to TEM and EDX elemental mappings (Fig. 1 and S2), the presence of homogeneously distributed PtCu alloys with diameters of ~1.0 nm was clearly identified in PtCu/CeO₂, whereas PtCu with diameters of ~2.5 nm was severely agglomerated on Al₂O₃ surface. This phenomenon could be ascribed to a strong interaction between PtCu and CeO₂, which not only effectively reduce size of PtCu alloy, but also promote its dispersion. The interplanar spacing of PtCu alloy over PtCu/CeO₂ was measured to be 2.20 Å in Fig. 1c, ranging between 2.09 Å of Cu (111) and 2.26 Å of Pt (111), which can be preliminarily assigned to the PtCu alloy with exposed (111) facets [33]. Moreover, CO-TPD shown in Fig. S3 demonstrated the strong Pt–Cu interactions present in PtCu/CeO₂.

3.2. Catalytic performance

3.2.1. Catalytic activity of VOC mineralization

To investigate the dependence of catalyst activity on the support and alloy composition, all the as-prepared catalysts were compared by their catalytic removal performance of cyclohexane. The complete mineralization temperature of PtCu/CeO₂ thermocatalytic cyclohexane showed 150 °C lower than that of PtCu catalyst (Fig. S4). Then, the effect of PtCu composition ratio on catalytic performance was explored. For simplicity, Al₂O₃ supported PtCu alloy (Pt/Cu molar ratio is 1:3 and 1:9) are respectively denoted as Pt₁Cu₃ and Pt₁Cu₉, while Al₂O₃ loaded with monometallic (Pt or Cu) nanoparticle is labeled as Pt or Cu catalyst. All these samples except Cu catalyst have a Pt loading of ~0.2 wt%. As the catalytic performance of cyclohexane degradation over Al₂O₃ can be negligible (Fig. 2a), the active component of these catalysts is monometal (Pt or Cu) and alloy particles, and Al₂O₃ only plays a carrying role to provide effective specific surface and mechanical strength for nanoparticles. The thermocatalytic mineralization of cyclohexane over Cu catalyst below 250 °C can be negligible (Fig. S4). However, when Cu was introduced into Pt particles (PtCu, Pt₁Cu₃ and Pt₁Cu₉), the synergistic effect between Pt and Cu occurred and then effectively promoted the thermocatalytic reaction of Pt catalyst under medium/low temperature (<250 °C), and PtCu catalyst exhibited the best initial performance under both thermocatalytic and photothermocatalytic conditions (Fig. 2a and S4). It is convenient to compare catalysts activity by using

reaction temperatures of T₁₀, T₅₀, and T₉₀ (temperatures of cyclohexane mineralization at 10%, 50% and 90%, respectively), listed in Table S2. PtCu/CeO₂ demonstrated an outstanding catalytic performance with a T₉₀ of 200 °C under simulated sunlight, which was 100 °C lower than that of PtCu catalyst (300 °C) and 50 °C lower than PtCu/CeO₂ in the dark (250 °C). To explore the intrinsic activity of catalysts, kinetic experiments were also conducted and the apparent activation energy (*E_a*) could be obtained for each sample from the slope of the Arrhenius plots (Fig. 2b). PtCu/CeO₂ under simulated sunlight presented the lowest *E_a* (35.8 kJ mol⁻¹), in comparison with those of PtCu/CeO₂ in the dark (38.3 kJ mol⁻¹), PtCu (36.7 kJ mol⁻¹), Pt₁Cu₃ (40.9 kJ mol⁻¹), Pt₁Cu₉ (45.5 kJ mol⁻¹) and Pt (66.2 kJ mol⁻¹) under simulated sunlight. This result was consistent with the catalytic activity results, as lower activation energy could reduce the reaction energy barrier, leading to a faster reaction rate [34]. Additionally, the long-term stability test at 250 °C with a total reaction time of 125 h indicated the excellent photothermocatalytic stability of PtCu/CeO₂ (Fig. S5), and carbon deposit over the used PtCu/CeO₂ investigated by C1s XPS spectra demonstrated its fantastic coke resistance (Fig. S6).

3.2.2. Catalytic performance of simultaneous removal of VOCs and soot

PtCu/CeO₂ with high coke resistance was then applied in simultaneously photothermocatalytic removal of cyclohexane and soot. Firstly, soot effect on the photothermal oxidation of cyclohexane without catalyst was explored in Fig. S7. When temperature was raised to 600 °C, only 8% of cyclohexane mineralization was observed, but it reached ~39% in the presence of soot, implying soot can promote photothermal mineralization of cyclohexane. Then, the thermocatalytic and photothermocatalytic degradation of cyclohexane and soot over PtCu/CeO₂ was compared (Fig. 2c and d). As temperature rose to 150 °C without light (PtCu/CeO₂, Dark), cyclohexane outlet concentration increased gradually due to the desorption of cyclohexane adsorbed on soot surface, while under simulated sunlight, cyclohexane was degraded by photothermocatalysis before it was desorbed, so that its outlet concentration kept going down (Fig. 2c). Additionally, the temperature of CO₂ production maximum shifted from 384 °C to 326 °C compared to that without light, indicating photocatalytic process of PtCu/CeO₂ can effectively promote catalytic mineralization of VOCs and soot (Fig. 2d).

By comparing transient behavior of PtCu, CeO₂ and PtCu/CeO₂ during temperature programmed reaction, it was found that photothermocatalytic degradation of both cyclohexane and soot over PtCu catalyst at the temperature below 170 °C can be negligible. For CeO₂ alone, cyclohexane can be degraded at 100 °C–250 °C (Fig. 2c), but the amorphous carbon and organic carbon on soot surface cannot be mineralized until temperature rose to 260 °C (Fig. 2d). As a result, CO₂ production over CeO₂ during 260 °C–400 °C was greater than that of PtCu/CeO₂. Therefore, it can be concluded that CeO₂ plays a major role in photothermocatalytic degradation of cyclohexane at low temperature region (<250 °C), while PtCu alloy dominated degradation at high temperature (>250 °C). Under photothermocatalytic synergistic effect between PtCu and CeO₂, the initiation temperature of both cyclohexane

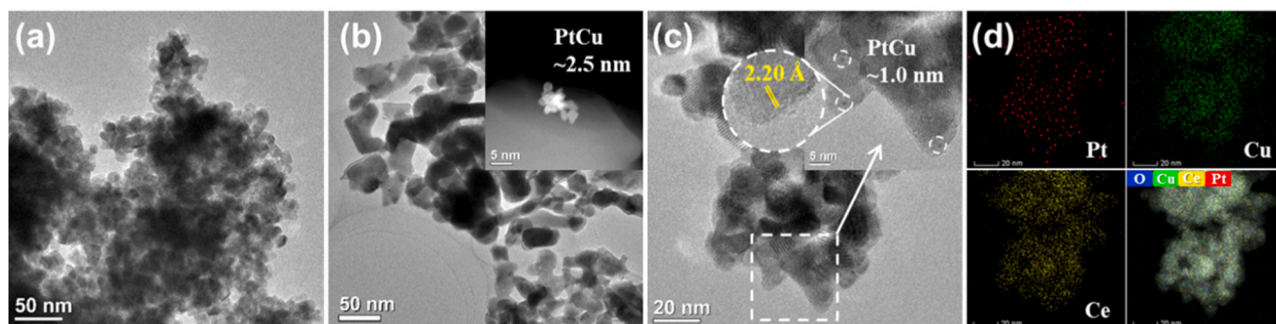


Fig. 1. TEM images of (a) CeO₂, (b) PtCu, (c) PtCu/CeO₂, and (d) HAADF images in STEM mode and EDX elemental mappings of PtCu/CeO₂.

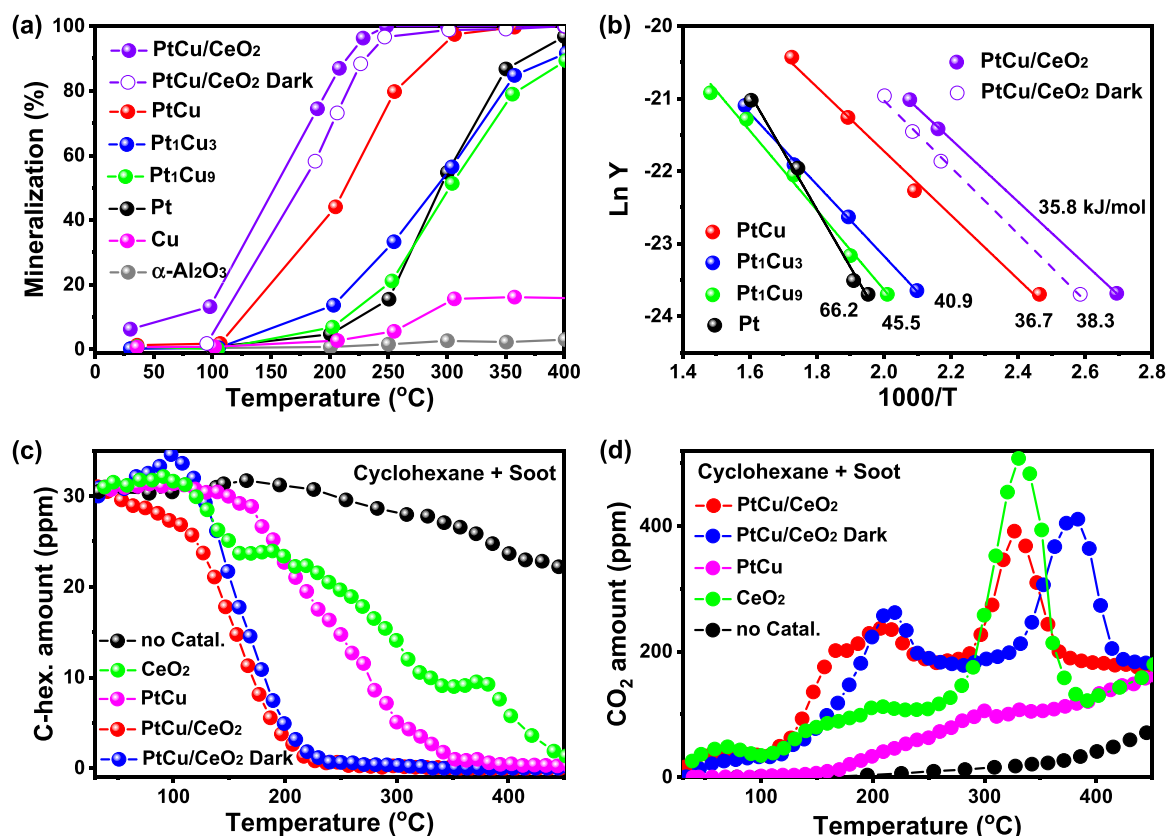


Fig. 2. (a, b) Initial activity and Arrhenius plots of catalysts for cyclohexane degradation; (c, d) The concentration of cyclohexane and CO₂ as a function of temperature over catalysts loosely mixed with soot.

and soot degradation is lowered. Besides, temperatures of soot mineralization at 90% ($T_{90, \text{soot}}$) with different catalysts demonstrated that PtCu/CeO₂ exhibited the best initial catalytic oxidation performance among catalysts reported in the literature (Table S4 and Fig. S8). Moreover, the stability test of used PtCu/CeO₂ for simultaneous removal of cyclohexane and soot again verified the good cyclic stability of PtCu/CeO₂ (Fig. S9).

3.3. Discussion on the high photothermocatalytic performance of PtCu/CeO₂

To gain insight into the reasons why high photothermocatalytic performance of the PtCu/CeO₂, its surface chemical states of elements and oxygen species were first analyzed with XPS. Apparent negative binding energy shifts of both Ce 3d and Cu 2p region in PtCu/CeO₂ compared with CeO₂ and PtCu catalyst (Fig. S10a and b), further confirmed there is a strong interaction between PtCu and CeO₂, which will be conducive to the formation of more low-valence Ce ions (Ce³⁺) and oxygen vacancies, and then facilitates catalytic oxidation reaction [35]. Cu 2p_{3/2} characteristic peak was fitted into one Gaussian peaks at 932.0 eV for PtCu/CeO₂ and 933.6 eV for PtCu, respectively assigned to Cu⁰ and Cu²⁺ [15], indicating Cu atoms on PtCu/CeO₂ are mainly metallic, but a small amount of oxidation states cannot be excluded. The actual Ce³⁺ content in PtCu/CeO₂ was estimated as 16.5% (Table S5), much higher than that of CeO₂ (13.6%). The O1s XPS spectra of both CeO₂ and PtCu/CeO₂ can be fitted with three Gaussian peaks at 529.3, 531.6 and 533.1 eV (Fig. 3a), assigned to lattice oxygen species (O_l), surface adsorbed oxygen species (O_s) and surface hydroxyls/adsorbed water (O_{-OH}), respectively [36]. All these surface oxygen species (O_l and O_{-OH}, such as O²⁻, O⁻ and hydroxyl group) are regarded as the dominant ROSs for redox reaction, and PtCu/CeO₂ showed much higher amount of surface oxygen (29.2%) than that of CeO₂ (26.0%), indicating

PtCu ultrafine alloy is beneficial to oxygen chemisorption, which will be participate in the subsequent activation and catalytic oxidation. Pt 4f XPS confirmed the coexistence of Pt⁰ (82.8%) and Pt²⁺ (Fig. S10c), and the small amount of Pt²⁺ can improve the valence stability of PtCu alloy and promote redox reaction of oxygen species on catalyst surface [37]. Moreover, the presence of Pt²⁺ in the alloy clusters indicates electrons donation from Pt to Cu, resulting in Cu²⁺ to Cu⁰ (Fig. S10b) [38], which provided more evidence that the stronger interaction between Pt and Cu in PtCu/CeO₂ than that in PtCu, leading to its high stability and dispersion of alloys. Besides, the characteristic Raman peaks of PtCu/CeO₂, including F2g band (α, 458 cm⁻¹), oxygen defect bands β (243 cm⁻¹) and γ (593 cm⁻¹), show an obvious negative wavenumber in comparison with that of CeO₂, and the bands become wider (Fig. S10d). This is because the partial incorporation of Pt/Cu causes lattice deformation of CeO₂ (Fig. S1), thus forming more oxygen vacancies in PtCu/CeO₂. Oxygen vacancies play an important role in promoting photothermocatalytic reaction, which will be discussed below by the results of optical and redox property characterization.

The optical properties of PtCu/CeO₂ including light response and charge separation were evaluated and illustrated in Fig. 3b and c. PtCu catalyst had negligible light absorption, while both CeO₂ and PtCu/CeO₂ had a distinct near-ultraviolet absorption band with the edge of 430 nm. Moreover, PtCu/CeO₂ displayed stronger light absorption but weaker PL intensity than CeO₂, suggesting the enhanced light harvesting and improved charge separation in PtCu/CeO₂. This is because more oxygen vacancies and PtCu ultrafine alloy (form a Schottky barrier with CeO₂) onto PtCu/CeO₂, induces more photoexcitation processes and acts as electron acceptor to effectively inhibit rapid recombination of photo-generated charge, thus promoting more charges to generate and then transfer to the catalyst surface to participate in the reaction.

The reducibility of PtCu/CeO₂ under dark and illumination was investigated by H₂-TPR (Fig. 3d). Only one small peak α at 382 °C can be

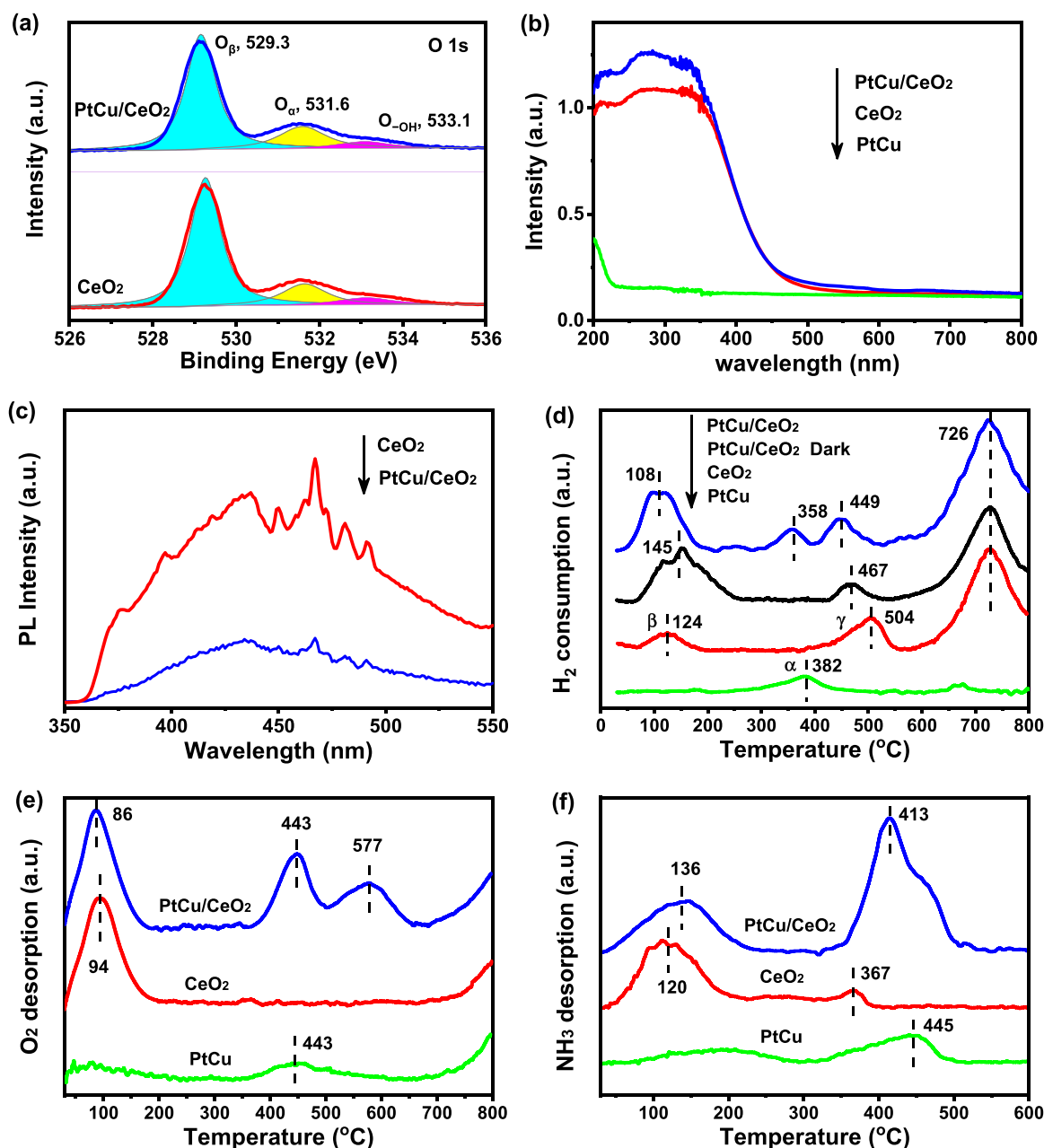


Fig. 3. (a) O1s XPS spectra; (b,c) UV-vis diffuse reflectance and photoluminescence spectra of catalysts with an excitation of 280 nm; (d) H₂-TPR profiles; (e,f) O₂-TPD and NH₃-TPD profiles in darkness.

observed on PtCu catalyst under illumination, caused by the reduction of PtCuO_x. CeO₂ under illumination showed three broad peaks, one denoted as peak β at 124 °C is related to the reduction of surface oxygen species onto CeO₂ (such as chemisorbed O²⁻, O⁻ and hydroxyl group), and the other peak γ located at 504 °C is associated with the reduction of Ce⁴⁺ to Ce³⁺ ions in the outermost layer. The third peak observed with the maxima at 726 °C is attributed to the reduction of lattice oxygen and the subsurface layer of Ce⁴⁺ [39]. Compared with PtCu and CeO₂ catalysts, all H₂-TPR peaks (α, β and γ) of PtCu/CeO₂ under illumination shifted to lower temperatures. This phenomenon illustrates that ROSs interacting with PtCu alloy could be reduced easily at low temperature, and the strong interaction between PtCu and CeO₂ lattice can increase the reducibility of ceria surface oxygen due to the relaxing Ce-O bond strongly interacting with well-dispersed PtCu ultrafine alloys [40]. Besides, the distinct peak α cannot be detected by PtCu/CeO₂ in the dark, probably due to the overlap of peak γ at 467 °C, and PtCu/CeO₂ under

illumination shows the significantly decreased reduction temperature and increased H₂ consumption for peaks β and γ in comparison with that in the dark. The above results imply that the combined effects of illumination and the strong MSI of PtCu/CeO₂ greatly accelerate reduction of surface/subsurface oxygen species and facilitate activation or mobility of oxygen species, thus enhancing its photothermocatalytic performance.

For getting insight into adsorption and activation of oxygen on PtCu/CeO₂, and further investigating its lattice oxygen mobility, O₂-TPD was also performed (Fig. 3e). It is well known that the desorption of surface adsorbed oxygen species with increasing temperature changes by the following procedures: surface adsorbed peroxy species (O₂⁻, below 200 °C) → surface adsorbed monatomic species (O⁻, 200–500 °C) → surface lattice oxygen (O²⁻, 500–700 °C) → bulk lattice oxygen (beyond 700 °C) [41], and the physically adsorbed oxygen has been removed by purging Ar before O₂-TPD analysis. PtCu catalyst did not show obvious

O_2^- desorption peak below 200 °C, where both CeO_2 and $PtCu/CeO_2$ revealed the distinct O_2^- peak of almost the same area, and the latter's shifted towards lower temperature. These indicate $PtCu$ ultrafine alloy did not affect oxygen storage capacity of CeO_2 for weakly chemisorbed oxygen, but can lower oxygen desorption temperature and then promote oxygen migration and diffusion during catalytic process. Compared with $PtCu$ catalyst, the oxygen desorption peak intensity and area of $PtCu/CeO_2$ at 443 °C, associated with O^- , increased significantly. Besides, a new desorption peak of $PtCu/CeO_2$ appeared at 577 °C, which is related to surface lattice oxygen, while neither $PtCu$ nor CeO_2 existed, indicating the strong MSI enhances the migration and activation of lattice oxygen in the outer layer of CeO_2 [42]. All the above results demonstrate the oxygen activation capacity and oxygen mobility of $PtCu/CeO_2$ are enhanced after loading $PtCu$ ultrafine alloy, which effectively promote its photothermocatalytic reaction.

It is well known that the surface acidity of catalyst directly affects its catalytic activity [43]. Generally, the reaction involving C-H bond cleavage requires weak acid sites, while C-C bond breaking needs strong acid sites [44]. NH_3 -TPD analysis is an ideal tool for characterizing the catalyst surface acidity. For CeO_2 -based catalyst, the NH_3 desorption peak appeared at low temperature (α peak, below 250 °C) is corresponded to weak acid site, while high temperature peak (β peak, beyond 300 °C) is assigned to strong acid sites [45]. As Fig. 3f shows, the α peak area of $PtCu/CeO_2$ becomes larger in comparison with CeO_2 , indicating the amount of its weak acid sites increased. Besides, the β peak signal of $PtCu/CeO_2$ is obviously higher than that of CeO_2 and $PtCu$ catalyst, implying that there are more strong acid sites in $PtCu/CeO_2$. Therefore, $PtCu/CeO_2$ with abundant acid sites is more conducive to promoting the cleavage of C-H bond and C-C bond, and then accelerating the catalytic degradation of organic pollutants.

3.4. The pros and cons of soot on the photothermocatalytic process

The results in Fig. S7 have confirmed that soot has a certain positive effect on the photothermocatalytic mineralization of VOCs as its carbon structure characteristics of light absorption and heat transfer. The outlet concentration of cyclohexane and CO_2 as a function of temperature during photothermocatalytic removal of cyclohexane over $PtCu/CeO_2$ mixed with and without soot particles was tested and compared in Fig. 4a and b. Under the photothermocatalytic condition of less than 150 °C, cyclohexane degradation efficiency is higher upon exposure of $PtCu/CeO_2$ with soot, which again confirms the promotion of soot on catalytic oxidation of VOCs. This is due to the abundant active sites on soot surface and its unique photothermal properties, which promotes the photosensitive reaction of soot to generate active free radicals [46]. Under the joint effect of $PtCu/CeO_2$ and soot, the rapid photothermocatalytic degradation of cyclohexane at relatively low temperature (<150 °C) is promoted. TG curve shows soot lost ~3.2% of its weight by heating to 150 °C at 5 °C min⁻¹ (Fig. S11), implying some surface species of soot (including surface functional groups and surface carbon) were oxidized. During the photothermocatalytic process of 150 °C–200 °C, cyclohexane degradation over $PtCu/CeO_2$ mixed with soot is lower than that of soot absence (Fig. 4a), but more CO_2 is produced in the presence of soot (Fig. 4b), further demonstrating the amorphous carbon and organic carbon on soot surface are mineralized at this stage. The depletion of functional groups on soot surface affects its ability to activate oxygen and generate active free radicals, and the partially degraded soot is easy to occupy the surface-active site of $PtCu/CeO_2$ and then passivate its surface states [47], thus reducing the photothermocatalytic activity of VOCs upon exposure of $PtCu/CeO_2$ mixed with soot. Moreover, the effect of soot on the surface structure of $PtCu/CeO_2$, such as the amount of Ce^{3+} and surface oxygen species, was explored by XPS spectra (Fig. S12) and summarized in Table S5. The

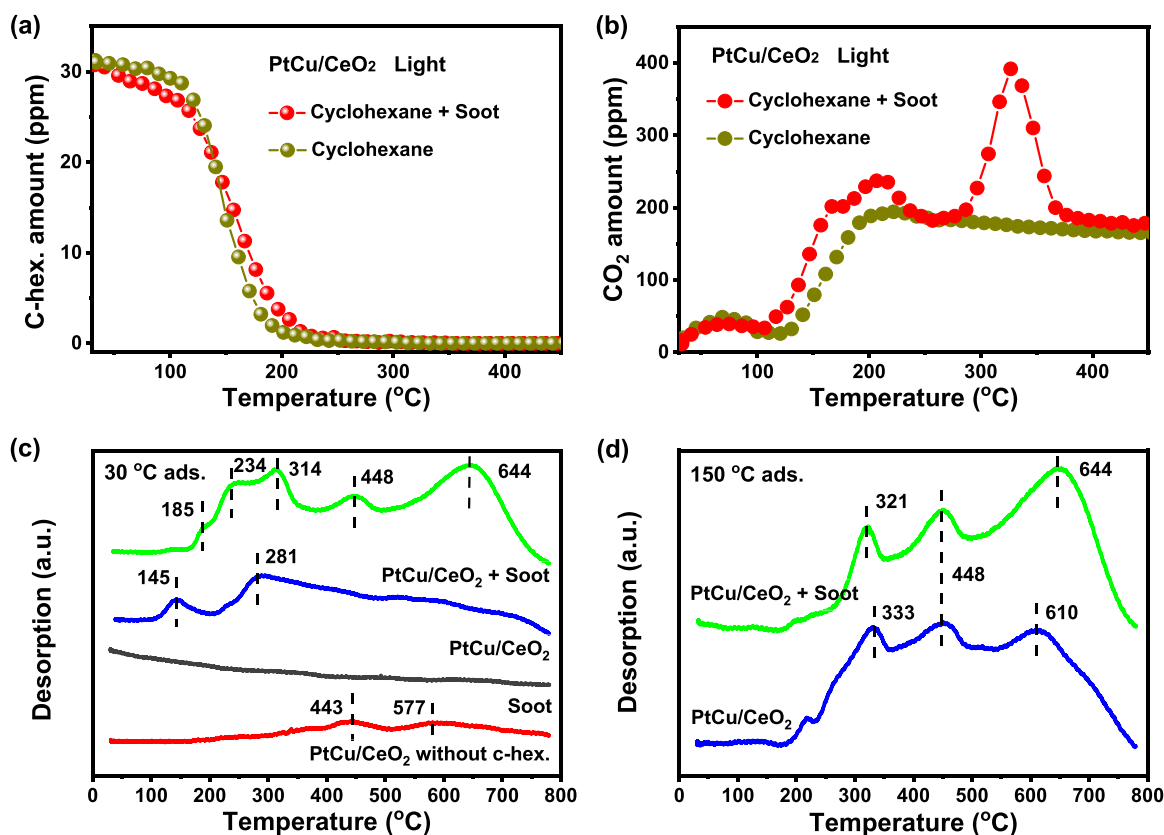


Fig. 4. (a, b) The concentration of cyclohexane and CO_2 as a function of temperature and (c, d) Cyclohexane-TPD profiles of $PtCu/CeO_2$ mixed with/without soot under light.

sample of PtCu/CeO₂ mixed with soot before and after photo-thermocatalytic degradation of cyclohexane carried out from 30 °C to 150 °C at a rate of 1 °C min⁻¹, are respectively labeled as PtCu/CeO₂ +soot (fresh) and PtCu/CeO₂ +soot (used). In contrast with the fresh PtCu/CeO₂, PtCu/CeO₂ +soot (fresh) showed a slight lower Ce³⁺ content, but higher surface oxygen species (O_α and O_{-OH}) amount, demonstrating soot increases the oxygen active site on catalyst surface due to its abundant oxygen-containing functional groups. However, the content of both Ce³⁺ and surface oxygen species of PtCu/CeO₂ +soot (used) decreased significantly, again proving the partially degraded soot during photothermocatalytic oxidation reaction would occupy and passivate the surface-active site of PtCu/CeO₂.

The photothermocatalytic process is a dynamic *in-situ* surface reaction process. To investigate the essential effect of soot on photothermocatalytic performance of PtCu/CeO₂, *in-situ* cyclohexane-TPD under illumination was used to evaluate the adsorption capacity and photothermocatalytic activity of PtCu/CeO₂ mixed with or without soot (Fig. 4c). PtCu/CeO₂ without pre-adsorption of cyclohexane shows two small broad peaks, one at 443 °C and another at 577 °C, which is respectively related to the adsorbed monatomic species (O⁻) and surface lattice oxygen according to O₂-TPD results (Fig. 3e), suggesting 150 °C purification pretreatment could not remove the surface adsorbed O⁻ onto PtCu/CeO₂. Besides, no obvious cyclohexane-TPD peak was detected over soot, indicating cyclohexane cannot be chemically adsorbed on the pure soot, but only physical adsorption. The desorption of surface species as a function of temperature by the following procedures: weakly chemisorbed cyclohexane (α, 100–200 °C) → strongly chemisorbed cyclohexane and volatile degradation intermediates/products (β, 200–350 °C) → CO₂ produced by the reaction of surface adsorbed O⁻ with refractory degradation intermediates (γ, 350–500 °C) → CO₂ produced by surface lattice oxygen with refractory degradation intermediates/soot (δ, beyond 500 °C). By withdrawing the exhaust gas of cyclohexane-TPD into GC analysis at 50 °C intervals, it was confirmed that the desorption tail gas above 350 °C mainly contained CO₂.

After the pre-adsorption of cyclohexane at 30 °C (Fig. 4c), the α peak temperature of PtCu/CeO₂ mixed with soot is lower than that without it, suggesting soot promote cyclohexane adsorption onto PtCu/CeO₂ catalyst, which largely enhanced the activity for cyclohexane oxidation. Besides, two broad β peaks are observed over PtCu/CeO₂ mixed with soot, but only one occurred in soot absence, and the first β peak of the former has the lowest temperature, which implies that the initiation temperature of strongly chemisorbed cyclohexane oxidation over PtCu/CeO₂ can be decreased by soot. Moreover, PtCu/CeO₂ mixed with soot shows the obvious peak γ and δ, but none can be detected in the absence of soot, indicating that soot inhibits the deep oxidation of cyclohexane at a relatively low temperature (200–350 °C). After the pre-adsorption of

cyclohexane at 150 °C (Fig. 4d), no obvious α peak can be observed over PtCu/CeO₂ mixed with and without soot, revealing that cyclohexane adsorbed at 150 °C undergo the strong chemisorption on PtCu/CeO₂ surface. Compared with soot absence, the β peak temperature of PtCu/CeO₂ mixed with soot was lower and its peak area was also smaller, again confirming that soot can reduce the initiation temperature of cyclohexane over PtCu/CeO₂, but inhibit its ability of deep oxidation into CO₂.

For further exploring the nature of positive and negative effect of soot, DFT calculations were also performed. A model of PtCu onto CeO₂ [111] surface was optimized to investigate adsorption energies of OH, O₂, and cyclohexane molecules over catalysts mixed with or without soot (Fig. 5). For the fresh catalysts, the adsorption energies of OH, O₂, and cyclohexane on PtCu/CeO₂ [111] were calculated and ranked by OH (−4.72 eV) > O₂ (−2.82 eV) > cyclohexane (−1.13 eV), indicating that both OH and O₂ were more easily adsorbed and then activated on catalyst surface, follow by generating ROSS to oxidize cyclohexane. Besides, the adsorption energy of soot on PtCu/CeO₂ [111] was obtained as −0.05 eV, which is a small value, but it also demonstrates that soot could be weakly adsorbed on PtCu/CeO₂ [111], hence exhibiting a certain effect on the redox properties. After soot mixing, the calculated adsorption energies of OH (−4.57 eV) and O₂ (−2.68 eV) were reduced, while the adsorption energy of cyclohexane (−1.61 eV) was obviously enhanced, implying that soot occupied part of active sites on catalyst surface. This led to a decrease in the activation of OH and O₂, meanwhile its porous carbon structure promoted the adsorption of cyclohexane. This phenomenon would accelerate cyclohexane degradation, but also have a negative effect on its deep oxidation, just like the result of cyclohexane-TPD in Fig. 4. All above results reveal the trade-off between the positive effect of soot and its poisoning effect exists in simultaneously photothermocatalytic removal of VOCs and soot over PtCu/CeO₂.

4. Conclusion

In summary, CeO₂ supported low-dose PtCu ultrafine alloy catalyst with high coke resistance was developed for efficiently simultaneously photothermocatalytic removal of VOCs and soot. Further the trade-off between the positive effect of soot and its poisoning over PtCu/CeO₂ in this photothermocatalytic oxidation were unraveled. By combining activity evaluation, XPS, DRS, PL, Raman, H₂-TPR, O₂-TPD and NH₃-TPD characterization, the photothermocatalytic improvement is demonstrated to be due to increased activation and mobility of oxygen onto PtCu/CeO₂, and its abundant acid sites. According to the results from XPS, *in-situ* cyclohexane-TPD, and DFT calculations, the trade-off effects of soot in photothermocatalytic degradation were proposed as

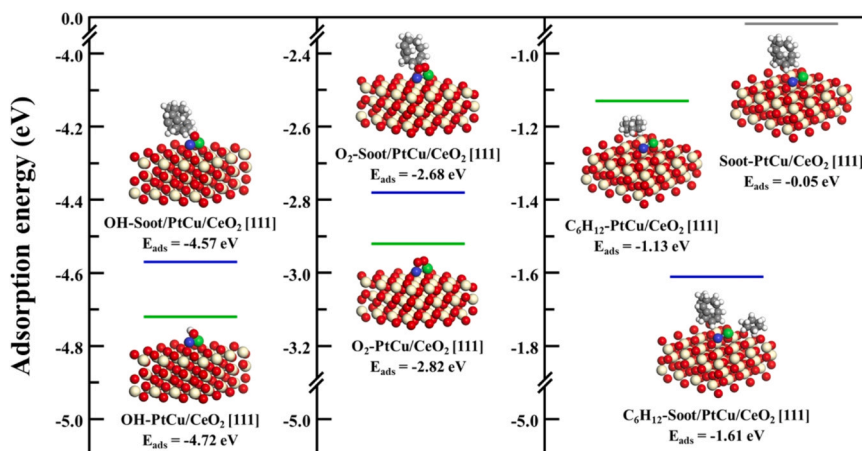


Fig. 5. Adsorption energy comparison of OH, O₂, and cyclohexane molecules on PtCu/CeO₂ [111] mixed with/without soot. The green line represents the fresh catalyst, while the blue one represents catalyst mixed with soot, and the gray line shows adsorption energy of soot on PtCu/CeO₂ [111].

follow: (1) the positive effect of soot derives from its unique properties of light absorption and heat transfer, and enhanced VOC adsorption, thus accelerating the photothermocatalytic degradation of VOCs; (2) the negative effect of soot is attributed to that the partially degraded soot would poison the surface-active site of PtCu/CeO₂ and weaken OH/O₂ adsorption, hence suppressing the deep oxidation of VOCs into CO₂. This work exemplifies a promising strategy to alloy catalyst developed to photothermocatalytic simultaneous removal of refractory VOCs and soot, and provide a deep understanding of the pros and the cons mechanism of soot in this photothermocatalytic process.

CRedit authorship contribution statement

Jiejing Kong: Methodology, Formal analysis, Writing – original draft. **Shengnan Song:** Methodology, Validation. **Weina Zhao:** Data curation, Formal analysis. **Zijie Yu:** Validation. **Ziwei Xiang:** Data curation. **Guiying Li:** Writing – review & editing. **Weiping Zhang:** Methodology, Validation. **Taicheng An:** Conceptualization, Supervision.

Declaration of Competing Interest

The authors declare that they have no known competing financial interests or personal relationships that could have appeared to influence the work reported in this paper.

Data availability

No data was used for the research described in the article.

Acknowledgements

This work was financially supported by National Natural Science Foundation of China (42007315, 22006023 and 42007327), Guangdong Basic and Applied Basic Research Foundation (2022A1515011465 and 2019A1515110413), Guangdong Provincial Key R&D Program (2022-GDUT-A0007), and Key-Area Research and Development Program of Guangdong Province (2019B110206002).

Appendix A. Supporting information

Supplementary data associated with this article can be found in the online version at doi:10.1016/j.apcatb.2023.123118.

References

- [1] S.X. Zheng, X.R. Zhou, Z.L. Tan, C. Liu, H. Hu, H. Yuan, S.N. Peng, X.M. Cai, Assessment of the global energy transition: Based on trade embodied energy analysis, *Energy* 273 (2023), 127274.
- [2] Y.R. Tan, Q.R. Zhu, Y.C. Zong, J.W. Lai, M. Salamanca, J. Akroyd, W.M. Yang, M. Kraft, The influence of alcohol, carbonate and polyethers as oxygenated fuels on the soot characteristics from a CI engine, *Fuel* 338 (2023), 127296.
- [3] P. Wu, X.J. Jin, Y.C. Qiu, D.Q. Ye, Recent progress of thermocatalytic and photothermocatalytic oxidation for VOCs purification over manganese-based oxide catalysts, *Environ. Sci. Technol.* 55 (2021) 4268–4286.
- [4] S.D. Liu, H.Y. Wang, S. Wang, Y.L. Dai, B. Liu, Y. Liu, F.X. Dang, K. Smith, X.W. Nie, S.D. Hou, Engineering morphology and Ni substitution of Ni₃Co_{3-x}O₄ spinel oxides to promote catalytic combustion of ethane: elucidating the influence of oxygen defects, *ACS Catal.* 13 (2023) 4683–4699.
- [5] J. Cain, P. Gassman, H. Wang, A. Laskin, Micro-FTIR study of soot chemical composition-evidence of aliphatic hydrocarbons on nascent soot surfaces, *Phys. Chem. Chem. Phys.* 12 (2010) 5206–5218.
- [6] W.J. Jin, G.R. Zhi, Y.Z. Zhang, L. Wang, S.C. Guo, Y. Zhang, Z.G. Xue, X.M. Zhang, J.H. Du, H. Zhang, Y.J. Ren, P. Xu, J.H. Ma, W.J. Zhao, L.F. Wang, R.C. Fu, Toward a national emission inventory for the catering industry in China, *Sci. Total Environ.* 754 (2021), 142184.
- [7] W. Zhang, Y. Chen, G. Zhang, X. Tan, Q.H. Ji, Z.W. Wang, H.J. Liu, J.H. Qu, Hot-electron-induced photothermal catalysis for energy-dependent molecular oxygen activation, *Angew. Chem. Int. Ed.* 60 (2021) 4872–4878.
- [8] J.W. Li, X.Q. Yang, C.R. Ma, Y. Lei, Z.Y. Cheng, Z.B. Rui, Selectively recombining the photoinduced charges in bandgap-broken Ag₃PO₄/GdCrO₃ with a plasmonic Ag bridge for efficient photothermocatalytic VOCs degradation and CO₂ reduction, *Appl. Catal. B-Environ.* 291 (2021), 120053.
- [9] Y.J. Hao, Y.G. Ma, X. Zhang, J.J. Li, S.F. Wang, X.M. Chen, F.T. Li, Unraveling the importance between electronic intensity and oxygen vacancy on photothermocatalytic toluene oxidation over CeO₂, *Chem. Eng. J.* 433 (2022), 134619.
- [10] A. Gaenzler, M. Casapu, P. Vernoux, S. Lorient, F. Aires, T. Epicier, B. Betz, R. Hoyer, J. Grunwaldt, Tuning the structure of platinum particles on ceria InSitu for enhancing the catalytic performance of exhaust gas catalysts, *Angew. Chem. Int. Ed.* 56 (2017) 13078–13082.
- [11] M. Salaeve, A. Salaeve, T. Kharlamova, G. Mamontov, Pt-CeO₂-based composites in environmental catalysis: A review, *Appl. Catal. B-Environ.* 295 (2021), 120286.
- [12] Z.S. Wang, M. Cheng, Y. Liu, Z.W. Wu, H.Y. Gu, Y. Huang, L.Z. Zhang, X. Liu, Dual-atomic-site catalysts for molecular oxygen activation in heterogeneous thermo-/electro-catalysis, *Angew. Chem. Int. Ed.* (2023). DOI10.1002/anie.202301483.
- [13] C.T. Yang, G. Miao, Y.H. Pi, Q.B. Xia, J.L. Wu, Z. Li, J. Xiao, Abatement of various types of VOCs by adsorption/catalytic oxidation: A review, *Chem. Eng. J.* 370 (2019) 1128–1153.
- [14] Y.F. Zheng, K.X. Fu, Z.H. Yu, Y. Su, R. Han, Q.L. Liu, Oxygen vacancies in a catalyst for VOCs oxidation: synthesis, characterization, and catalytic effects, *J. Mater. Chem. A* 10 (2022) 14171–14186.
- [15] J.J. Kong, G.Y. Li, M.C. Wen, J.Y. Chen, H.L. Liu, T.C. An, The synergic degradation mechanism and photothermocatalytic mineralization of typical VOCs over PtCu/CeO₂ ordered porous catalysts under simulated solar irradiation, *J. Catal.* 370 (2019) 88–96.
- [16] W.P. Zhang, G.Y. Li, H.L. Liu, J.Y. Chen, S.T. Ma, M.C. Wen, J.J. Kong, T.C. An, Photocatalytic degradation mechanism of gaseous styrene over Au/TiO₂@CNTs: Relevance of superficial state with deactivation mechanism, *Appl. Catal. B-Environ.* 272 (2020), 118969.
- [17] C. Garcia-Fernandez, S. Picaud, M. Rayez, J. Rayez, J. Rubayo-Soneira, First-principles study of the interaction between NO and large carbonaceous clusters modeling the soot surface, *J. Phys. Chem. A* 118 (2014) 1443–1450.
- [18] J. Zhang, L. Wang, B.S. Zhang, H.S. Zhao, U. Kolb, Y.H. Zhu, L.M. Liu, Y. Han, G. X. Wang, C.T. Wang, D.S. Su, B. Gates, F.S. Xiao, Sinter-resistant metal nanoparticle catalysts achieved by immobilization within zeolite crystals via seed-directed growth, *Nat. Catal.* 1 (2018) 540–546.
- [19] Y. Feng, L. Dai, Z. Wang, Y. Peng, E. Duan, Y. Liu, L. Jing, X. Wang, A. Rastegarpanah, H. Dai, J. Deng, Photothermal Synergistic Effect of Pt₁/CuO-CeO₂ Single-Atom Catalysts Significantly Improving Toluene Removal, *Environ. Sci. Technol.* 56 (2022) 8722–8732.
- [20] H.Y. Wang, E. Ruckenstein, Partial oxidation of methane to synthesis gas over alkaline earth metal oxide supported cobalt catalysts, *J. Catal.* 199 (2001) 309–317.
- [21] I. Son, S. Kwon, J. Park, S. Lee, High coke-resistance MgAl₂O₄ islands decorated catalyst with minimizing sintering in carbon dioxide reforming of methane, *Nano Energy* 19 (2016) 58–67.
- [22] J.J. Kong, Z.W. Xiang, G.Y. Li, T.C. An, Introduce oxygen vacancies into CeO₂ catalyst for enhanced coke resistance during photothermocatalytic oxidation of typical VOCs, *Appl. Catal. B-Environ.* 269 (2020), 118755.
- [23] Z.Y. Liu, P. Lustemberg, R. Gutierrez, J. Carey, R. Palomino, M. Vorokhta, D. Grinter, P. Ramirez, V. Matolin, M. Nolan, M. Ganduglia-Pirovano, S. Senanayake, J. Rodriguez, In Situ Investigation of Methane Dry Reforming on Metal/Ceria(111) Surfaces: Metal-Support Interactions and C-H Bond Activation at Low Temperature, *Angew. Chem. Int. Ed.* 56 (2017) 13041–13046.
- [24] X. Zhou, K. Li, Y.X. Lin, L. Song, J.C. Liu, Y. Liu, L.L. Zhang, Z.J. Wu, S.Y. Song, J. Li, H.J. Zhang, A. Single-Atom, Manipulation approach for synthesis of atomically mixed nanoalloys as efficient catalysts, *Angew. Chem. Int. Ed.* 59 (2020) 13568–13574.
- [25] M. Marcinkowski, M. Darby, J.L. Liu, J. Wimbles, F. Lucci, S. Lee, A. Michaelides, M. Flytzani-Stephanopoulos, M. Stamatakis, E. Sykes, Pt/Cu single-atom alloys as coke-resistant catalysts for efficient C-H activation, *Nat. Chem.* 10 (2018) 325–332.
- [26] H.Y. Liang, B.F. Jin, M. Li, X.X. Yuan, J. Wan, W. Liu, X.D. Wu, S. Liu, Highly reactive and thermally stable Ag/YSZ catalysts with macroporous fiber-like morphology for soot combustion, *Appl. Catal. B-Environ.* 294 (2021), 120271.
- [27] V. Malmberg, A. Eriksson, S. Török, Y.L. Zhang, K. Kling, J. Martinsson, E. Fortner, L. Gren, S. Kook, T. Onasch, Relating aerosol mass spectra to composition and nanostructure of soot particles, *Carbon* 142 (2019) 535–546.
- [28] J.J. Wei, Y.C. Wang, Effects of biodiesels on the physicochemical properties and oxidative reactivity of diesel particulates: A review, *Sci. Total Environ.* 788 (2021), 147753.
- [29] C. Han, Y.C. Liu, J.Z. Ma, H. He, Key role of organic carbon in the sunlight-enhanced atmospheric aging of soot by O₂, *PNAS* 109 (2012) 21250–21255.
- [30] H.X. Sun, Y.Z. Li, J.Y. Li, Z.Q. Zhu, W.T. Zhang, W.D. Liang, C.H. Ma, A. Li, Facile Preparation of a Carbon-Based Hybrid Film for Efficient Solar-Driven Interfacial Water Evaporation, *ACS Appl. Mater. Interfaces* 13 (2021) 33427–33436.
- [31] Q. Li, J. Shang, T. Zhu, Physicochemical characteristics and toxic effects of ozone-oxidized black carbon particles, *Atmos. Environ.* 81 (2013) 68–75.
- [32] J. Kugai, T. Moriya, S. Seino, T. Nakagawa, Y. Ohkubo, H. Nitani, Y. Mizukoshi, T. A. Yamamoto, Effect of support for PtCu bimetallic catalysts synthesized by electron beam irradiation method on preferential CO oxidation, *Appl. Catal. B-Environ.* 126 (2012) 306–314.
- [33] J.Y. Wang, Y.Z. Li, J.T. Zhao, Z. Xiong, Y.C. Zhao, J.Y. Zhang, PtCu alloy cocatalysts for efficient photocatalytic CO₂ reduction into CH₄ with 100% selectivity, *Catal. Sci. Technol.* 12 (2022) 3454–3463.
- [34] Y.F. Zheng, Q.L. Liu, C.P. Shan, Y. Su, K.X. Fu, S.C. Lu, R. Han, C.F. Song, N. Ji, D. G. Ma, Defective ultrafine MnO_x nanoparticles confined within a carbon matrix for

- low-temperature oxidation of volatile organic compounds, *Environ. Sci. Technol.* 55 (2021) 5403–5411.
- [35] Q.Y. Wang, Y.X. Li, A. Serrano-Lotina, W. Han, R. Portela, R.X. Wang, M. Banares, K. Yeung, Operando Investigation of Toluene Oxidation over 1D Pt@CeO₂ Derived from Pt Cluster-Containing MOF, *J. Am. Chem. Soc.* 143 (2021) 196–205.
- [36] X. Chen, S.C. Cai, E.Q. Yu, J.J. Li, J. Chen, H.P. Jia, Photothermocatalytic performance of ACo₂O₄ type spinel with light-enhanced mobilizable active oxygen species for toluene oxidation, *Appl. Surf. Sci.* 484 (2019) 479–488.
- [37] Q.Q. Wu, M.Z. Jing, Y.C. Wei, Z. Zhao, X.D. Zhang, J. Xiong, J. Liu, W.Y. Song, J. M. Li, High-efficient catalysts of core-shell structured Pt@transition metal oxides (TMOs) supported on 3DOM-Al₂O₃ for soot oxidation: The effect of strong Pt-TMO interaction, *Appl. Catal. B-Environ.* 244 (2019) 628–640.
- [38] Y. Feng, L. Wei, Z.W. Wang, Y.X. Liu, H.X. Dai, C. Wang, H.C. Hsi, E. Duan, Y. Peng, J.G. Deng, Boosting catalytic stability for VOCs removal by constructing PtCu alloy structure with superior oxygen activation behavior, *J. Hazard. Mater.* 439 (2022), 129612.
- [39] Z. Zhao, J. Ma, M. Li, W. Liu, X.D. Wu, S. Liu, Model Ag/CeO₂ catalysts for soot combustion: Roles of silver species and catalyst stability, *Chem. Eng. J.* 430 (2022), 132802.
- [40] J. Lee, D. Jo, J. Choung, C. Kim, H. Ham, K. Lee, Roles of noble metals (M = Ag, Au, Pd, Pt and Rh) on CeO₂ in enhancing activity toward soot oxidation: Active oxygen species and DFT calculations, *J. Hazard. Mater.* 403 (2021), 124085.
- [41] Y.L. Zheng, W.Z. Wang, D. Jiang, L. Zhang, X.M. Li, Z. Wang, Ultrathin mesoporous Co₃O₄ nanosheets with excellent photo-/thermo-catalytic activity, *J. Mater. Chem. A* 4 (2016) 105–112.
- [42] Y.C. Xiao, H. Li, K. Xie, Activating lattice oxygen at the twisted surface in a mesoporous CeO₂ single crystal for efficient and durable catalytic CO oxidation, *Angew. Chem. Int. Ed.* 60 (2021) 5240–5244.
- [43] L.M. Zhang, Y.J. Gong, Y.L. Zhai, T. Ma, C.F. Xu, S.W. Zuo, L.R. Zheng, J. Zhang, L. Ping, Creation of CuOx/ZSM-5 zeolite complex: healing defect sites and boosting acidic stability and catalytic activity, *Catal. Sci. Technol.* 10 (2020) 4981–4989.
- [44] Z. Huang, S. Cao, J. Yu, X. Tang, Y. Guo, Y. Guo, L. Wang, S. Dai, W. Zhan, Total Oxidation of Light Alkane over Phosphate-Modified Pt/CeO₂ Catalysts, *Environ. Sci. Technol.* 56 (2022) 9661–9671.
- [45] Z.Y. Fei, C. Cheng, H.W. Chen, L. Li, Y.R. Yang, Q. Liu, X. Chen, Z.X. Zhang, J. H. Tang, M.F. Cui, X. Qiao, Construction of uniform nanodots CeO₂ stabilized by porous silica matrix for 1,2-dichloroethane catalytic combustion, *Chem. Eng. J.* 370 (2019) 916–924.
- [46] N. Moteki, K. Adachi, S. Ohata, A. Yoshida, T. Harigaya, M. Koike, Y. Kondo, Anthropogenic iron oxide aerosols enhance atmospheric heating, *Nat. Commun.* 8 (2017) 15329.
- [47] S. Yu, H. Yun, Y. Kim, J. Yi, Carbon-doped TiO₂ nanoparticles wrapped with nanographene as a high performance photocatalyst for phenol degradation under visible light irradiation, *Appl. Catal. B-Environ.* 144 (2014) 893–899.